Advanced Polymer Processing

Edited by
Lianxiang Ma, Chuangsheng Wang
and Weimin Yang

ttp TRANS TECH PUBLICATIONS

Advanced Polymer Processing

Edited by
Lianxiang Ma
Chuangsheng Wang
Weimin Yang

Advanced Polymer Processing

Selected, peer reviewed papers from the
Advanced Polymer Processing International Forum,
Qingdao, China, 19-21 August 2009, APPF 2009

Edited by

Lianxiang Ma, Chuangsheng Wang and Weimin Yang

Scientific.Net

Trans Tech Publications Ltd
Kapellweg 8
CH-8806 Baech
Switzerland
https://www.scientific.net

Vols. 87-88 of
Advanced Materials Research
SSN print 1022-6680
ISSN web 1662-8985

Full text available online at *http://www.scientific.net*

***Distributed** worldwide by*

Trans Tech Publications Ltd
Kapellweg 8
CH-8806 Baech
Switzerland

Phone: +41 (44) 922 10 22
Fax: +41 (44) 922 10 33
e-mail: sales@scientific.net

Preface

Polymer material is one of the three raw materials in today's world-metal, inorganic non-metallic and organic polymer materials. It has been widely used in the fields of economic development, scientific & technological innovation and is playing a more and more important role. As China's modern manufacturing has been forging ahead from a big producing country to a powerful manufacturing state, the knowledge innovation and technical process in advanced polymer processing field are changing with each new day. It is developing towards high performance, function and environmental-friendliness rapidly and lots of new scientific researches are raised for the science and engineering communities at the same time.

The "2009 Advanced Polymer Processing (Qingdao) Int'l Forum" surrounded the developmental trend of advanced polymer processing technology closely, made all-around, multi-angle communication and discussion on the challenges and opportunities for Chinese polymer material manufacturing industry by the national and abroad famous experts, professors and many well-known competitiveness in the market at all levels.

For the purpose of further communication, we put the papers that selected for this forum to be published in the proceeding.

Lianxiang Ma
Qingdao University of Science & Technology
August 25 , 2009

APPF2009

Organizing Committee

Chairman	Lianxiang Ma (China)
Vice-chairman	Chuangsheng Wang (China) Weimin Yang (China)
Secretary General	Tikun Shan (China)
Members	Zhengpin Liao (China) Lin Xu (china) Linda (USA) Limper (Germany) Haberstroh (Germany)

Table of Contents

Preface

Committee

Analysis on the Hydroplaning of Aircraft Tire
Y.S. Wang, J. Wu and B.L. Su 1

Dynamic Compressive Response and Failure Behavior of Basalt Fibers Polymer Functional Composites Embedded with ZnO Whiskers
W. Zhou, L.J. Wen, X.X. Zhang, X. Wang, J.L. Rong and H.B. Jin 7

Preparation and Controlled-Release Analysis of Ethyl Cellulose – Moxa Leaf Powder Solution Microcapsules
Y. Zhang, L. Li, W.M. Au, Z.M. Yang, G.R. He, S.X. Deng, Z.H. Yang, J.W.Y. Chung and T.K.S. Wong 11

Numerical Simulation of Temperature Field in Barrel of Injection Molding Machine during Induction Heating Process Based on ANSYS Software
S.J. Chang, P.C. Xie, X.T. He and W.M. Yang 16

Adsorption Properties of Chemical Crosslinked Polymer Gel
X.Y. Hu and Y.B. Chen 22

Investigation of Performance Advantages of Internal Circulation Two-Platen Injection Molding Machine
Z.W. Jiao, P.C. Xie, Z.Y. Yan, W.M. Yang and X.T. Wang 27

Visual Experiment Study on the Influence of Mold Structure Design on Injection Molding Product's Defects
P.C. Xie, B. Du, Z.Y. Yan, Y.M. Ding and W.M. Yang 31

Synthesis and Characterization of Novel Amphiphilic Fluorinated Triblock Copolymer
X.D. Tang, N.F. Han and D.J. Zhou 36

Interaction of Polymer and Solvent in Chemical Crosslinked Polymer Gel
X.Y. Hu and Y.B. Chen 41

Synthesis and Property of Photo- and Temperature- Dual-Responsive Amphiphilic Block Copolymers
X.D. Tang, N.F. Han and D.J. Zhou 47

Research on High-Powered Brazing Diamond Saw for Cutting Vehicle Tyre
B.J. Ma and Z.A. Xu 52

Research on Tribological Properties of Micro-Vehicle Clutch's Friction Material
J.C. Lv, Y.M. Mo and L.N. Pan 58

Experimental Study on Mold Separations of Plastic Injection Molding Machines with Different Clamping Units
P.P. Zhang, P.C. Xie, D. Hua and W.M. Yang 64

The Melting and Recrystallization Behavior of Poly(ethylene Terephthalate)/SiO_2 Nanocomposites Studied by Step-Scan DSC
C. Liu, K. Zheng, X.Y. Yao, X. Zhang, X.L. Liu, R.X. Wang and X.Y. Tian 69

Preparation of Polysulfone Membranes Using Ionic Liquid [C_{16}mim][SCN] as a Pore-Former and Plasticizer
Y.M. Zhao, X.L. Hu, J.Y. Yu and P. Guan 74

Synthesis and Properties of Molecularly Imprinted Composite Membranes of Roxithromycin
J.Y. Yu, X.L. Hu, C.C. Jiao, Y.M. Zhao and W.W. Yang 80

Thermal Conductivity of Nature Rubber Filled with Carbon Black
Y. He, H.T. Li and L.X. Ma 86

Influence of Mineral Admixtures on the Performance of Polymer Modified Porous Concrete
F. Xu, M.K. Zhou, W.G. Shen and B.X. Li 92

Carbon Nanofibers from Pyrolysis Flame and Research on the Affecting Factors
Y.C. Liu, B.M. Sun, T.K. Shan and Z.Y. Ding 98

Carbon Nanotubes Preparation Using Carbon Monoxide from the Pyrolysis Flame
B.M. Sun, Y.C. Liu and Z.Y. Ding 104

Experimental Study on Property of Rubber Composites Filled With Carbon Nanotubes
Z.P. Wang 110

Heat Transfer during Rotational Molding of a Single Axis Device
Y.L. He and Y.M. Ding 116

Influences of Preparative Conditions on Properties of Erythromycin-Molecularly Imprinted Membrane
P. Guan, X.L. Hu and Y.M. Zhao 119

Research of Microprofile Extrusion
H. Wang, Z.H. Fu and D.G. Yao 125

Quantum Chemistry Theoretical Studies on Molecular Structures of Polybutadiene
M. Zhang, Z.X. Huang and M.X. Shi 130

Study on Oil Resistance Properties of Flexible PVC/PNBR Blends
Y. An, W.M. Yang, Y.M. Ding, Y. Liu and J. Tan 134

Thermal Conductivity and Mechanical Properties of Silicone Rubber Filled with Different Particle Sized SiC
Y. He, Z.C. Chen and L.X. Ma 137

Water-Activated Bacterial Cellulose-Based Electrorheological Fluids and Electromechanical Response of Artificial Muscle Based on Electrorheological Fluids and Siloxane Gel
N. Xu and D.M. Jia 143

Fatigue Analysis of the New Stirring Kneader Shafts Using ANSYS
J.Q. Xu and Z.M. Fan 149

Two New Thermotropic Liquid Crystalline Polyesters and their Composites: Synthesis and Characterization
C.J. Zhang, Z.X. Huang, M.X. Shi and M. Zhang 154

Pressure Function Method in Tyre Structure Design
J.Z. Wang, D.G. Chang, Z.X. Xin and L. Li 160

Effect of Activated Zinc Oxide on the Property of Sole Rubber
T.K. Shan, T. Zhuang and L.L. Zhou 167

Optimum Design of Spindle Used in Tire Building Machine
D.G. Chang and X.F. Wang 172

3D Finite Element Simulation of Transient Temperature Field for Rapid Electrical Heating Cycle Injection Mold
X.P. Li, G.Q. Zhao and Y.J. Guan 177

The Application of Harmonic Response Analysis in Different-Speed Mixer Design
Z.M. Fan, W.G. Sun and J. Xu 183

Comparison of Human Articular Cartilage and Polyvinyl Alcohol Hydrogel as Artificial Cartilage in Microstructure Analysis and Unconfined Compression
F. Li, Y.L. Su, D.F. Shi and C.T. Wang 188

Virtual Prototype Design System of Tripod Universal Joints
D.G. Chang, F.Q. Yang and H. Chen 194

Research of Thermal Conductivity and Tensile Strength of Carbon Black-Filled Nature Rubber
Y. He, Z. Yin, L.X. Ma and J.P. Song 200

The Optimal Design of Oscillating Oil Cylinder Mechanism of Tire Building Machine
Z.M. Meng, Y.B. Qiao and Z.M. Fan 206

A New Type Device of Thread Locking Connection of Pillar Flat Vulcanizing Machine
Z.M. Meng, Y. Zhang and Y.B. Qiao 211

On-Line PVT Properties of Amorphous Polymers
J. Wang, P.C. Xie, Y.M. Ding and W.M. Yang 216

Study on the End-Point Control of Holding Phase during Injection Molding
J. Wang, P.C. Xie, Y.M. Ding and W.M. Yang 222

Preparation and Properties of Nano-Hydroxyapatite Modified Nylon Composites
L.Y. Zheng, Z.M. Liu and Y.J. Zhao 228

Dispersion Polymerization of Acrylamide and Acrylic Acid in Aqueous Media
J. Lu, B. Peng, M.Y. Li and M.Q. Lin 233

Properties of HDPE/UHMWPE Blown Films
J.D. Zuo, S.M. Liu and J.Q. Zhao 239

A Study on the Optimization and Application of All Radial Truck Tire Building Process Technology
Z.H. Li, S.L. Yang, P. Xia, Z.F. Li, Y.Q. Liu and S.Z. Wu 244

Analysis of Melting Process and Numerical Simulation of Pure UHMW-PE Pipe Based on Molding in Barrel Technology
J.H. Qin, C.H. Liu, W.F. Gao and C.H. Yu 250

Experimental Research on Carbon Black Flowing in Pneumatic Conveying System
Z.H. Li, Y.Q. Liu, P. Xia and L. Ma 256

Development of Durable Softening and Water-Repellent PP/HDPE Heat-Bondable Composite Fiber
S.Y. Sun, Q.F. Zhao and Y. Xue 265

Hyperbranched Polymers as Novel Flame Retardant Material
J. Borah, G.Y. Lin and C.S. Wang 271

Effects of Different Structure Rotors on Mixing Process and Quality of Short Fiber-Rubber Composite Material
C.S. Wang, D.W. Zhang and H.G. Bian 277

Preparation and Thermal Properties of Phosphorus-Containing Copolyester Nanocomposites with Carbon Nanotube
Q.F. Zhao, S.Y. Sun, X.W. Jiang, M.H. Qu and Y.Z. Wang 282

Research of Temperature Control System Based on Fuzzy Control Algorithm for Mixer
C.S. Wang and F.H. Zhou 288

Research on the Curing Behaviour of an Epoxy/nmSiO_2 Nanocomposite System
C.S. Wang, Y.X. Fu and G.Y. Lin 293

Synthesis of Conducting Polyaniline Using Compound Oxidant
H. Huang, J.Q. Xu and Z.C. Guo 300

Research on the Key Technology of Precision Injection Molding Equipment for Light Guide Plate
P.C. Xie, G. Gou, Z.X. Wen, Y.M. Ding and W.M. Yang 306

Investigation of the Structural Change of Doped Polyaniline during Heat Treatment
H. Huang and Z.C. Guo 311

Experimental Study on Manufacturing Process of Short Fiber-Rubber Composite Material Using New Type Six-Wing Synchronous Rotor
D.W. Zhang and C.S. Wang 317

Three Dimension Fluid Field of Mixer with Synchronous Rotors
H.G. Bian, C.W. Fu and D.W. Zhang 323

Research on Mechanical Performance of Roof Tiles Made of Tire Powder and Waste Plastic
Y. Liu, W.M. Yang and M.F. Hao 329

Prediction of Process-Induced Residual Stress for Laminated Composites with Metallic Plate
J. Shi, Q. Zeng, X.D. He, R.G. Wang and Z.H. Hu 333

Heat Transfer of Water Film Outside the Vertical Helix Tube with Hydrophilic Nanolayer
Y.Y. Wang and Z.R. Zhang 339

Preparation and Properties Study on the Composites of Polypropylene and Polyphenylene Sulfide Filled by Modified Molybdenum Disulfide
J.Q. Zhang, H.X. Feng and J.H. Qiu 345

Study of Rheology of Flame-Retardant Copolyester Nanocomposites
Q.F. Zhao, X.W. Jiang, S.Y. Sun, M.H. Qu and Y.Z. Wang 351

Bioadhesive from Distiller's Dried Grains with Solubles
C.Q. Fang, R. Auras and S.E. Selke 357

Preparation and Electrical Conductivity of Composites of PA66 Filled with Carbon Nanotubes
F.C. Tsai, P. Li, X.P. Shang, N. Ma, L.C. Tsai and J.T. Yeh 363

The Model Reconstruction of Carbon Black/Rubber Composites' Heat Generation Ratio Based on Levenberg-Marquardt BP Algorithm
Z.Z. Yu and L.X. Ma 369

CAE Analysis of the Big-Size Injection Mold of Rear Bumper
Q.Z. Yin, R.K. Song, X. Zhang and B. Qi 375

Research on Microchannel of PMMA Microfluidic Chip under Various Injection Molding Parameters
B.Y. Jiang, Y. Liu, C.P. Chu and Q.J. Qiu 381

A Study in the Adsorption Behaviors of Cr (VI) on Crosslinked Amphoteric Starches Synthesized through Using the Microwave Radiation Method
L.X. Zou, Q.C. Liu, Q. Xu and J.H. Rong 387

The Mechanical and it Combined with Enzymatic Preparation Methods of Microfibrillated Cellulose
W.S. Chen, H.P. Yu, Y.X. Liu and Q. Li 393

An Improved Mixing-Extruding Machine for Polyblends
L. Li and C.S. Wang 398

Influence of Fine Content of Carbon Black Pellets during Pneumatic Conveying on Rubber and Mixing Process
Y. Li 405

An Experimental Method for the In-Plane Deformation Measurement in a Sample of Transparent Polymeric Material
X.L. Li, B. Liu, X.J. Li, Y.H. Qie, J.B. Sang and H.P. Jia 411

Characterization of Amorphous Silicon Thin Films Deposited on Upilex-s Polyimide Substrates for Application in Flexible Solar Cells
Y.G. Li and D.X. Du 416

Biodegradable Poly(Lactic Acid)/Organic-Montmorillonite Nanocomposites: Preparation and Characterization
N.L. Chen, H.X. Feng, H.M. Luo, D. Zhao and J.H. Qiu 422

PP/LDH Nanocomposites via Melt-Intercalation: Synergistic Flame Retardant Effects, Properties and Applications in Automobile Industries
P. Ding, S.F. Tang, H. Yang and L.Y. Shi 427

Preparation of Polyacrylamide Nanofibers by Electrospinning
L. Liu, W.W. Gu, W.T. Xv and C.F. Xiao 433

Studies on the Properties of Banana Fibers-Reinforced Thermoplastic Cassava Starch Composites: Preliminary Results
X.Z. Mo, Y.X. Zhong, C.Q. Liang and S.J. Yu 439

The Study on Buckling Deformation of Composite Pressure Vessel Based on Acoustic Emission Signals
Z.H. Hu, H.J. Liu, R.G. Wang, X.D. He and L. Ma 445

Expert System of Precise Injection Molding Process Optimization Based on Moldflow Software
P.C. Xie, B. Du, Z.Y. Yan, Y.M. Ding and W.M. Yang 451

Structure and Property of PGMA/Wood Composite
Y.F. Li, Y.X. Liu, J.T. Shi and G. Li 456

Research on the Thermal Oxidation and Ultraviolet Radiation Aging of Nano-ZnO/NR Composite
T. Zhuang, T.K. Shan and L.L. Zhou 462

Analysis and Comparison of Vapor and Liquid Deposition of Pyrrole on Wool Fiber
X. Jin, Y.Y. Wang and C.F. Xiao 468

Research on the Adjustable LAVAL Nozzle during Pneumatic Conveying
D.M. Jiao 474

Physical Properties of Poly(urethane-methacrylate)s Plastic Sheets Produced from Different Polyols
L.J. Gao, L.M. Zhou, S.M. Fang, H. Zheng, M. Hu and C.S. Liu 481

Impact on Tire Performance with Improvement of Semisteel Meridian Tire Lamination Processing
C.S. Wang, P. Fu, S.H. Li and Y.D. Jiang 487

The Experimental Research of SMR/SBR Inner Tube with RIIR
X.K. Zeng, C.S. Wang, H.G. Bian and L. Guo 493

Preparation of Anion Modified Montmorillonite-Polystyrene Nanocomposite by Suspension Polymerization
Y. Wang, H.X. Feng and J.H. Qiu 499

Effect of Vulcanization and Shaping Process on Radial Force Variation of TBR Tire
P. Fu, C.S. Wang, D.W. Zhang, H.G. Bian and Z. Pu 504

Research Method of the Rubber's Plasticization Technological Parameter Optimize on Open Mill by Neural Network
G.Z. Wang 509

Structure and Properties of Chitosan Containing Polyacrylic Acid Hydrogel Grafted SMS Nonwovens
X.P. Zhuang, W.J. Deng and B.W. Cheng 513

The Steady-State Temperature Field Analysis of the 3D Rolling Tire Based on Adina FEA Software
J. Li, Y. He and Z.C. Chen 518

Polymer Material Application in Cold Insulation Structures
X.L. Luo and B. Li 524

Periodic Mixing Performance in a Square Cavity for Different Frequencies
B.P. Xu, Y.J. Liu and J.P. Qu 529

Dependence of Thermal Conductivity of Carbon Black Filled Rubber on Several Factors
J.P. Song and L.X. Ma 536

Research on the Polymer Ultrasonic Plastification
B.Y. Jiang, J.L. Hu, W.Q. Wu and S.Y. Pan 542

A Study on Influence of Resin Temperature on Filling Balance of Multi-Cavity Molds
J.B. Chen, C.Y. Shen and H. Yokoi 550

Morphology of Biodegradable Poly(hexamethylene Adipate)(PHMA) Nanofibers Prepared by Electrospinning
W.M. Kang, B.W. Cheng, Q.X. Li and X.P. Zhuang 555

Experiment Research on Maximum Power of the VIC Mixer
F.Q. Yang, C.S. Wang, G.Y. Song and J. Xu 561

Advanced Materials Research
ISSN: 1662-8985, Vols. 87-88, pp 1-6
doi:10.4028/www.scientific.net/AMR.87-88.1

Online: 2009-12-21

Analysis on the Hydroplaning of Aircraft Tire

Y.S. Wang[1] , J. Wu[1] and B.L.Su[1]

[1] Center for composite materials, Harbin Institute of Technology, China

wangys@hit.edu.cn

Keywords: Hydroplaning, Finite element method, Aircraft tire

Abstract. Aircraft tire is an important subassembly of aircraft, which is related to its safety tightly, especially for civil aircraft. Moreover, hydroplaning of aircraft tires is often a contributing factor in take-off and landing overrun and veeroff accidents. Therefore the study on them is imperative. For studying the hydroplaning of aircraft tire, a 2D finite element model of aircraft tire is developed by using TYABAS software, and then a 3D patterned tire model is presented. The hydroplaning of aircraft tire is analyzed by generally coupling an Eulerian finite volume method and an explicit Lagrangian finite element method. The hydroplaning speeds are investigated, which is a key factor of hydroplaning. Results indicated that the hydroplaning speed increases with the increment of inflation pressure; the hydroplaning speed decreases with the increment of the footprint aspect ratio.

Introduction

The project of civil aircraft is a momentous systems engineering for national industry, which is also represent the technology of the nation. Aircraft tire is an essential part for aircraft. The performance of aircraft tire is directly correlated to the safety of aircraft.

Hydroplaning of aircraft tires is often a contributing factor in overrun and veeroff accidents. Therefore hydroplaning of aircraft tires has been studied for many years. The majority of the current knowledge on hydroplaning was obtained in the 60's mainly by NASA studies [1]. When an aircraft is running on the wet runway at high speed, the water flow through the tire tread grooves gives rise to the hydrodynamic pressure. The occurrence of this hydrodynamic force deteriorates the tire traction efficiency because it decreases the tire contact force, so that the driving controllability and the braking performance become worse than those on the dry runway when it is landing. From a fluid dynamics point of view, the tire wet traction is characterized by the flow pattern of water drained through the tire grooves [2, 3], so that the detailed tread geometry should reflected into the tire modeling [4-6].

In this study, a finite element model for the hydroplaning analysis of aircraft tire is developed by utilizing TYABAS and ABAQUS software. Firstly, a 2D finite element model is developed to the inflated analysis of the aircraft tire. The 3D patterned aircraft tire is then modeled based on the finite element method. The dynamic deformation of the aircraft patterned tire rolling on the wet runway is formulated by Lagrangian method, which is approximated by an explicit finite element method. On the other hand, the water flow is assumed to be incompressible and inviscid and approximated by a first-order Eulerian finite volume method equipped with the flow boundary tracking algorithm. The highly complex interaction between the tire dynamic deformation and the water flow is effectively treated by generally coupling both approximation methods.

Finite Element Model

2D Model of Aircraft Tire. Figure 1(a) shows a schematic view of 2D aircraft tire material, which is composite of fibre-reinforced rubber (FRR) part and the remaining pure rubber part. It can be seen that the layers of FRR parts in the aircraft tire are more than other type of tires due to the large load of aircraft tire. Since the FRR parts are in the highly complex structure, their material models are chosen based upon the goal of the numerical simulation under consideration. In the static tire analysis, those parts are usually modeled using solid elements like rebar elements. But, in the dynamic tire analysis this full modeling requires extremely long CPU time, so the FRR parts are modeled as either composite membrane or composite shell [7]. Figure 1(b) shows the meshing of 2D aircraft tire. Figure 2 illustrates the modeling of belt layer in the underlying rubber matrix as a single layer composed of orthotropic surfaces in numerical simulation.

Rubbers are modeled by Moonley-Rivlin model in which the strain density function is defined by

$$U = C_{10}(I_1-3)+C_{01}(I_2-3)+(1/D_1)(J_{el}-1)^2 \qquad (1)$$

where U is the strain density, C_{10} and C_{01} are the rubber material constants determined from experiment, D_1 is a sort of penalty parameter controlling the rubber incompressibility, J_{el} is the elastic volume ratio[7].

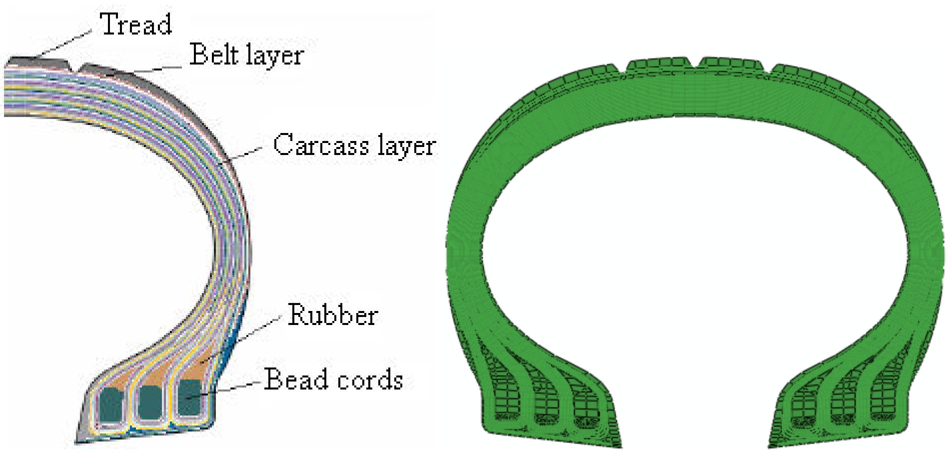

a) Model of material b) Meshing of aircraft tire

Fig.1 2D tire

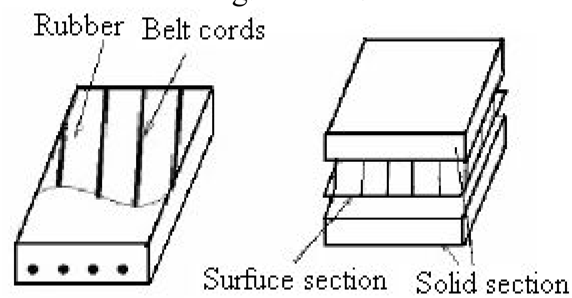

Fig.2 Modeling of belts

3D Model of Patterned Aircraft Tire. The 3D model of aircraft tire is transformed from the results of 2D tire mode Fig.3 (a) shows the finite element model of 3D patterned aircraft under the condition of hydroplaning. It can be seen that the mesh is just fined in the region against the runway for reducing the calculated time. Fig.3 (b) presents the contact press between tire and runway under the load of 15500 kg, the inflation pressure of 2.8 MPa and the rolling velocity of 300 km/h. It can be seen that the footprint length L is about 0.31 m; the footprint width W is about 0.19 m.

Hydroplaning

Hydroplaning Speed. When the aircraft tire rolls along a wet runway, it is squeezing water from under the footprint. This squeezing process generates water pressures on the surface of the tire footprint. At a critical speed the tire will be completely separated from the ground surface by a film of water. This speed is called the hydroplaning speed [8].

The total hydroplaning speed [1] is given as

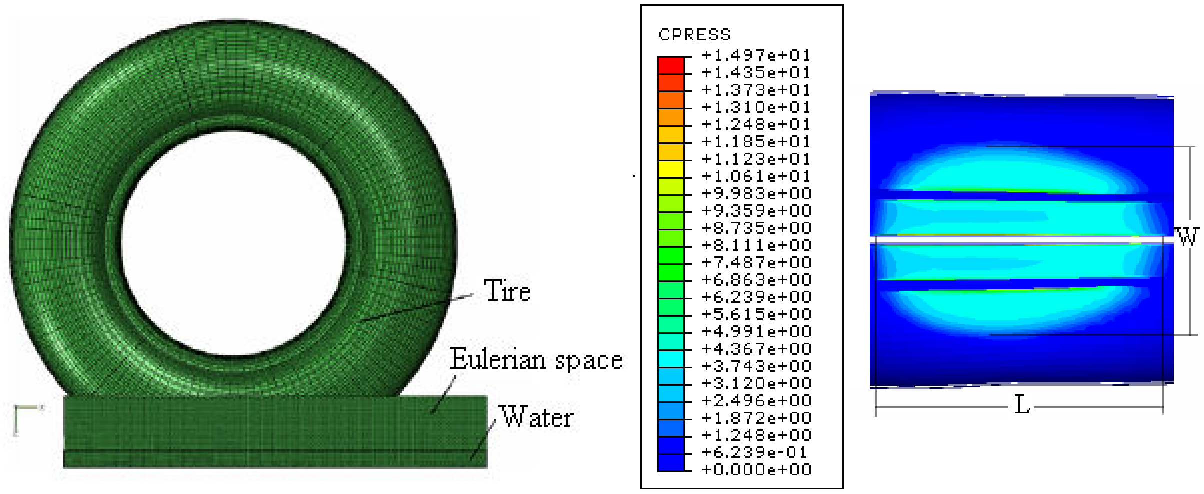

a) Meshing of 3D tire b) Contact press

Fig.3 3D patterned aircraft tire

$$v_{\mathrm{h}} = \sqrt{\frac{2}{C_{\mathrm{Lh}}}}\sqrt{\frac{p}{\rho}} \tag{2}$$

$$C_{\mathrm{Lh}} = \frac{2}{\lambda^2}\left(\frac{W}{L}\right)^2 \tag{3}$$

where v_{h} is the hydroplaning speed, C_{Lh} is the hydrodynamic lift coefficient, p the inflation pressure, ρ is the density of the water and λ is a constant, which depends on surface texture, tread of the tire and water depth.

Hydroplaning Process. When an aircraft is running on the wet runway, water collides with the tire grooves, while producing the hydrodynamic pressure and deforming the tire. As a result, the water flow and the tire dynamic deformation in the tire hydroplaning is strongly interacted to each other through the complex tire tread surface. Figure 4 shows a schematic representation of the three-zone concept [9] that classifies the region between the tire and the wet runway into three distinct parts: the hydrodynamic region I (tire is fully floated), the viscous hydrodynamic region II(tire is partially floated), and the complete contact region III (tire contacts with the ground directly). It is worthy noting that the occurrence of these regions depends on the water depth and the tire velocity.

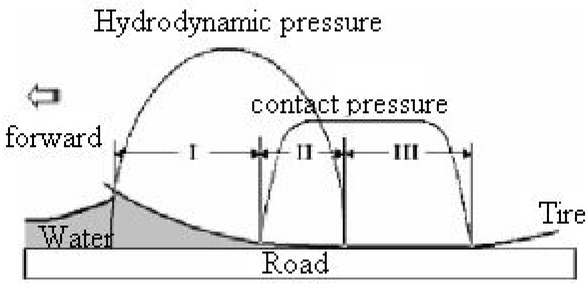

Fig.4 Three-zone concept [9] of hydroplaning

Discussions

Harrin suggests a value for λ of 1 based on some limited experimental data [10]. Similar values are found from theoretical calculations [11]. In Joyner's study, the constant λ is assumed to be equal to 0.85 [12]. However, detailed full-scale experiments are necessary to confirm this. So the constant λ varies between 0.85 and 1.

The hydroplaning speed v_h of the aircraft tire can be calculated from Eq.2 and Eq.3, which is given by

$$v_h = \frac{\lambda}{\kappa_{LW}} \sqrt{\frac{p}{\rho}} \tag{4}$$

where κ_{LW} is the footprint aspect ratio, which is the ratio of W and L.

The hydroplaning speed v_h varies between 256 km/h and 299 km/h. However, the rolling velocity of aircraft tire is 300 km/h, so it is in the hydrodynamic region I in this study.

The aircraft tire velocity is very high compared to general vehicle tire. It is in the hydrodynamic region I, because the velocity of aircraft tire is larger than hydroplaning speed under the rolling velocity of 300 km/h in this study. The hydroplaning process of aircraft under the rolling velocity of 300 km/h in simulation is also presented in Fig.5. The velocity vector of water is shown on the right side in the Fig.5. However there is no common method to derive the hydroplaning speed of aircraft tire from experiments. Figure 6 shows the real hydroplaning in a vehicle tire. It can be seen that it is in the viscous hydrodynamic region II due to the tire velocity, which is lower than that of aircraft tire.

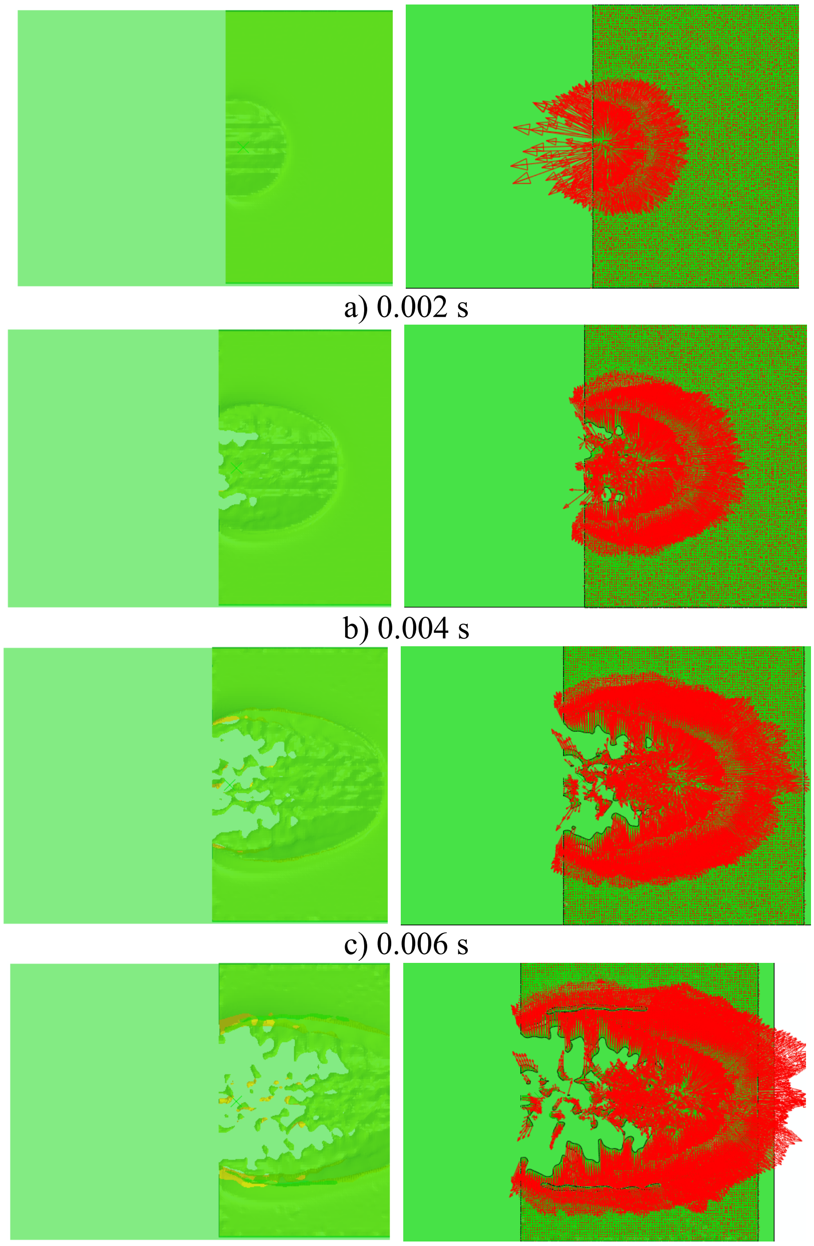

a) 0.002 s

b) 0.004 s

c) 0.006 s

d) 0.008 s

Fig.5 The process of hydroplaning process in simulation

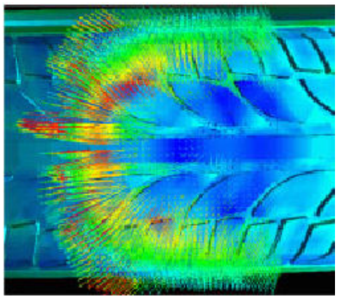

Fig.6 Real water flow in a vehicle tire [7]

From the Eq.4, it is presented that the hydroplaning speed increases when the inflation pressure increases; the hydroplaning speed decreases when the footprint aspect ratio increases. Some experimental data on hydroplaning speeds of aircraft tires as a function of inflation pressure for different tire types have been presented by G.W.H. vanes, which is shown in Fig.7

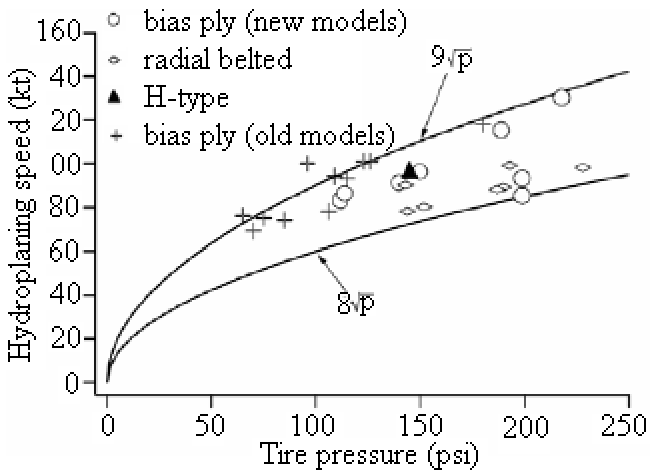

Fig.7 Experimental hydroplaning speeds [8]

Summary

Hydroplaning of aircraft tires is an important factor which should be considered into the aircraft safety. The hydroplaning process is simulated by coupling Lagrangian finite element method and Eulerian finite volume method. The simulation model of aircraft tire is developed by using ABAQUS. The hydroplaning speed is also investigated. Results indicate that the higher the velocity of tire, easier the hydroplaning to happen; the hydroplaning speed increases with the increment of inflation pressure; the hydroplaning speed decreases when the footprint aspect ratio increases.

References

[1] R.C. Dreher and W.B. Horne: NASA TND- 2056, 1963.

[2] D.F. Hays and A.L. Browne: *The Physics for Tire Traction-Theory and Experiment* (Plenum Press, New York 1974).

[3] R.W. Yeager and J.L. Tuttle: SAE Paper 720471, 1972.

[4] J.R. Cho, K.W. Kim and W.S. Yoo: International Journal of Advances in Engineering Software Vol. 35 (2004), p. 105-113.

[5] J.R. Cho, K.W. Kim, D.H. Jeon and W.S. Yoo: European Journal of Mechanics–A/Solids 24 (3) (2005), p. 519–531.

[6] J.R. Cho, H.W. Lee and W.S. Yoo: International Journal for Numerical Method in Engineering, Vol. 69 (2007), p. 1423-1445.

[7] Abaqus Software, Abaqus Theory Manual, Abaqus, USA, 2005.

[8] G.W.H. vanes. National Aerospace Laboratory NLR, NLR-TP-242, 2001, 1-10.

[9] A.L. Browne, H. Cheng and A.Kistler: Wear Vol. 20 (1972), p, 1-28.

[10] E.N.Harrin: NACA TN-4406, 1958.

[11] H. Bathelt: Automobil Technische Zeitschrift ATZ, Vol.75 (10) (1973), p. 368-374.

[12] U.T. Joyner and W.B. Horne: Aircraft Safety Seminar, Washington D.C., 1971.

Advanced Materials Research *Online: 2009-12-21*
ISSN: 1662-8985, Vols. 87-88, pp 7-10
doi:10.4028/www.scientific.net/AMR.87-88.7

Dynamic compressive response and failure behavior of basalt fibers polymer functional composites embedded with ZnO whiskers

W. Zhou[1,a], L.J. Wen[1,b], X.X. Zhang[1,c], X. Wang[2,d], J.L. Rong[2,e], H.B. Jin[2,f]

[1]The college of Quality and Technology Supervision, Hebei University, Baoding, China

[2]Aerospace Institute, Beijing Institute of Technology, Beijing, China

[a]zhouweihy@126.com, [b]wenlijuan22@163.com, [c]zhangxia@126.com, [d]wangxi@126.com, [e]rongjili@bit.edu.cn, [f]hbjinbit@126.com

Keywords: Dynamic response, Failure behavior, Functional composites, ZnO whiskers

Abstract. A type of basalt fibers polymer functional composites embedded with ZnO whiskers was prepared. The as-prepared composites exhibited good microwave absorption properties after the dispersion of ZnO whiskers in resin. The dynamic compressive properties of composites were investigated by the split Hopkinson pressure bar (SHPB) system. The macro- and micro-fracture morphology of composites was obtained by the scanning electron microscope (SEM). The experimental results showed that the as-prepared composites have excellent mechanical properties, and the compressive properties could be significantly affected by the strain rates in the in-plane direction, as well as in the normal direction. As the strain rate increased, the higher strength and elastic modulus are obtained. Under the dynamic compressive load in the normal direction, the main failure mode of composites is pure compression. On the other hand, longitudinal splitting and delamination of composites could be induced when loaded in the in-plane direction. The micro-interfacial crack, fiber fracture and plastic deformation of resin could be observed from the morphology of fractured composites.

Introduction

Recent years, fiber reinforced composites are being used increasingly due to excellent properties such as strong, stiff and light [1]. The good properties of composites are mainly attributed to excellent properties of fiber, resin and stuffing. Precious researches demonstrate that ZnO whiskers exhibit excellent microwave absorption properties [2] and good mechanical properties [3]. Therefore, the multi-functional properties of ZnO whiskers and the possibility of combining them with fiber composites have lead to the preparation of structural and functional composites.

Besides quasi-static mechanical properties [4], the study of dynamic mechanical properties is important for structural and functional composites because many of the applications are prone to service dynamic loading conditions such as high velocity impact from bird strikes or other foreign objects. The split Hopkinson pressure bar (SHPB) might be the most extensively experimental method for characterization of material under high strain rates [5]. Dynamic compressive strength and strain rate-dependent of polymeric composites were investigated by Sun et al. [6]. The results show that the stress-strain relation of composites is linear only when the sample is loaded in the longitudinal direction, whereas the nonlinear stress-strain relation in the off-axis direction. Similarly, Hosur et al. [7] studied the compressive behaviors of carbon/epoxy composites at high strain rate. Compare to static condition, the dynamic strength and stiffness exhibit considerable increase. Furthermore, Compressive response of glass-fiber reinforced polymeric composites was investigated by Shokrieh et al. [8]. They found that the compressive strength and modulus both increased with increasing the strain rate, the compressive strain to failure is generally insensitive to strain rate. But these researches mostly focused on the mechanical response of composites, whereas limited information with regard to the failure behavior and fracture morphology of composites [9].

In present work, a novel basalt fibers polymer functional composite was prepared by dispersing ZnO whiskers in resin matrix. The reflectivity of as-prepared composites was determined by the network analyzer. The compressive properties of as-prepared composites at high strain rates were investigated using SHPB. Furthermore, the microstructure and fracture morphology were performed utilizing the scanning electron microscope (SEM). The fracture and damage of the composites at high strain rates were discussed.

Materials and experimental procedure

Material description

ZnO whiskers were synthesized by combustion oxidization of metal zinc powders (purity: 99.99 wt %) without any catalyst. Using acetone as solvent, the ZnO whiskers, with the contents increased from 0 to 20 wt % along the normal direction gradually, were dispersed into the resin matrix (The weight ratio of the E-44 epoxy and 616 phenolic resin is about 1:1) homogeneously. After dispersion, the basalt fibers polymer functional composite was prepared by hand and hot-press at 448 K. The volume fraction of basalt fibers was about 65%, and the thickness of composites was about 12 mm.

Experimental procedure

In order to study the microwave absorption properties of composites, the 180mm×180mm specimens were prepared and the reflectivity of as-prepared composites was determined by the network analyzer. The compressive properties of as-prepared composites at high strain rates were investigated using SHPB. The specimens were machined into cylinders with diameter (D) 12mm and length 10mm in the normal direction, with diameter (D) 8mm and length 8mm in the in-plane direction by a lathe, respectively. In this process, the middle of composites should be ensured and the same ZnO contents could be obtained. Because of the friction between the specimen and pressure bar, the specimens should be polished before the test. According to Hopkinson's original one-dimensional stress wave theory and the signals of the strain gauges were recorded, the dynamic compressive properties of composites such as stress, strain rate and strain can be obtained. The microstructure and fracture morphology of specimens were investigated by SEM (HITACHI S-3500).

Results and discussions

Microwave absorption properties

The reflectivity of pure basalt fibers composites and as-prepared composites embedded with ZnO whiskers are shown in Fig.1 (a) and (b), respectively. The measured results show that as-prepared composites exhibited good microwave absorption properties after the embedment of ZnO whiskers, and the maximum microwave absorption of composites is up to 9.32dB at the frequency of 16.45 GHz. It could be attributed to excellent microwave absorption properties of ZnO whiskers [2]. The as-prepared composites could be used radar absorbing materials and shielding materials.

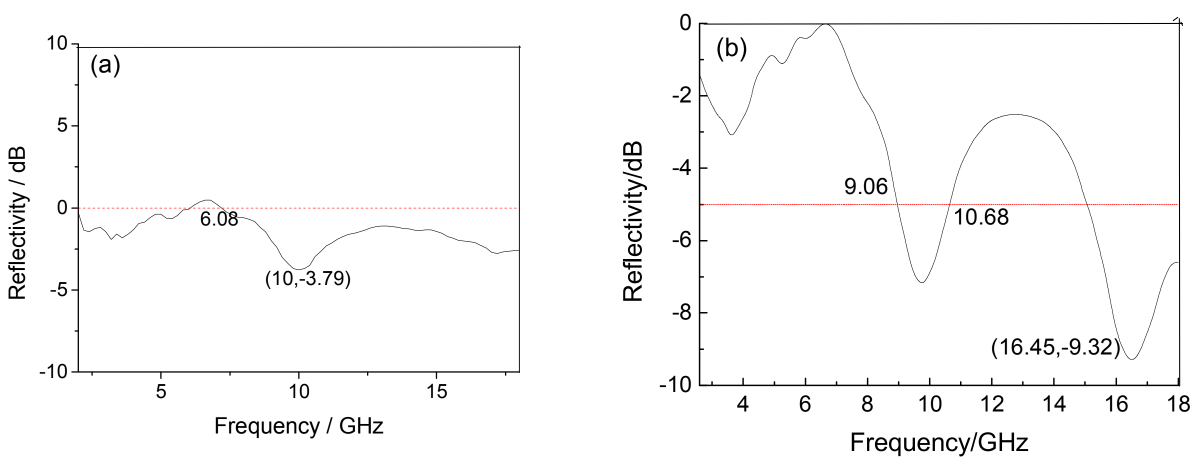

a. pure basalt fibers composites b. composites embedded with ZnO whiskers

Fig. 1 The reflectivity of composites

Dynamic compressive properties

According to a series of dynamic tests, the stress-strain relationships of as-prepared composites in the two different loading directions are shown in Fig.2. The results show that the compressive response of composites is very sensitive to the loading rate. From Fig.2 (a), as the strain rates increased from 495 S^{-1} to 932 S^{-1}, the maximum strength increased from 312.29 MPa to 418.54 MPa, the elastic modulus increased from 30.25 GPa to 62.67 GPa. As the strain rates increased from 1551 S^{-1} to 2055 S^{-1}, the maximum strength increased from 591.45 MPa to 657.23 MPa, the elastic modulus increased from 7.17 GPa to 8.88 GPa, the ultimate strain reduced from 0.083 to 0.074, as shown in Fig.2 (b). Because of high strength, high strain rate was performed in the normal direction. But, the compressive strength and ultimate strain at the in-plane direction and the normal direction could be compared similarly. The results show that the compressive strength and ultimate strain in the in-plane direction are obviously lower than those in the normal direction, whereas the higher elastic modulus in the in-plane direction is obtained. It could be attributed to the damage is always caused firstly at the inferior interface between fiber, whiskers and matrix. Shearing stress is replaced by compressive stress at these interfaces when loaded in the normal direction.

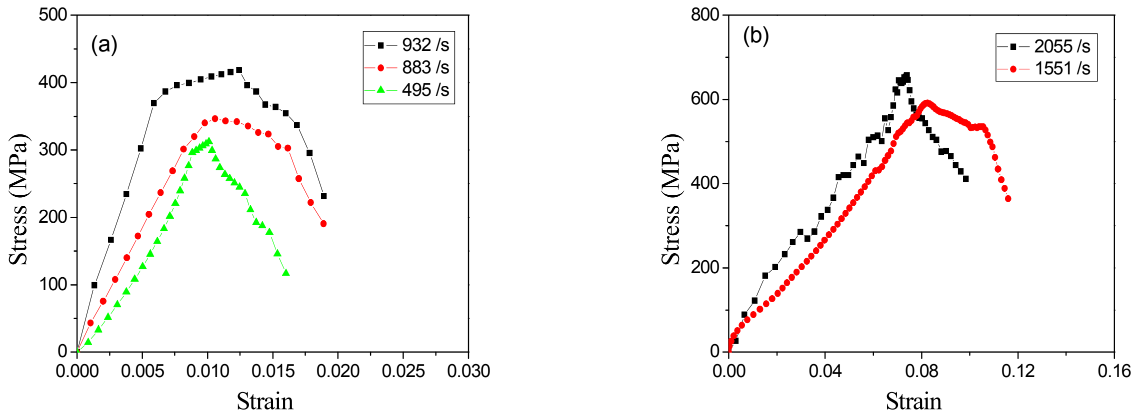

a. in the in-plane direction b. in the normal direction

Fig. 2 Dynamic compressive stress-strain relationship of as-prepared composites

Compressive failure morphology and fracture mechanism

The basic failure modes of fiber polymer composites are longitudinal splitting, shear crippling and pure compression. Under the dynamic compressive load, the typical macroscopic fracture and damage of as-prepared composites are shown in Fig.3. From Fig.3 (a), because the composites have no enough time to respond and stress concentration was produced, longitudinal splitting could be obtained. On the other hand, because no shearing stress exist at the interface of fiber and resin, pure compression could be produced when loaded in the normal direction as shown in Fig.3(b).

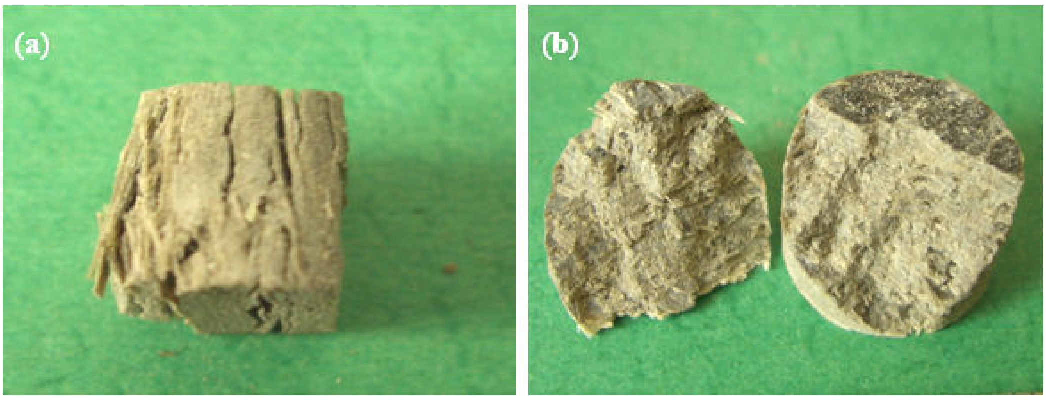

a. longitudinal splitting b. pure compression

Fig. 3 Macroscopic fracture and damage of as-prepared composites

According to results of SEM, the typical microscopic failures of as-prepared composites are shown in Fig.4. Interfacial cracks along specific fracture section are found evidently from the Fig.4 (a). From Fig.4 (b), because of shear failure, the fracture of fiber is brittle. At the same time, deformation of resin is shown in Fig.4 (c). The plastic deformation of resin could absorb energy, and the dynamic mechanical properties could be strengthened. Furthermore, ZnO whiskers could contribute to the good mechanical properties of composites. Under the dynamic load, heat could be generated, the compressive failure of composites become complex.

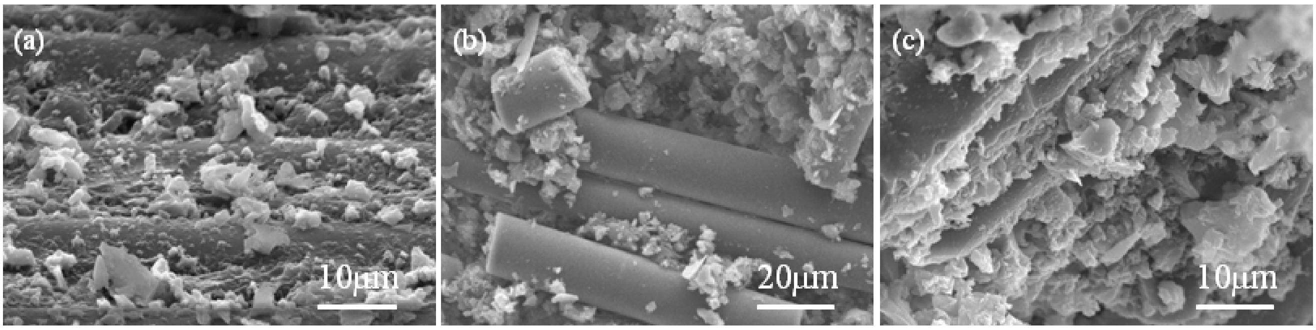

a. interfacial crack b. fiber fracture c. deformation of resin

Fig. 4 Microscopic failure of as-prepared composites

Summary

In summary, the novel basalt fibers polymer functional composites exhibited good microwave absorption properties and dynamic mechanical properties. The compressive properties of as-prepared composites are significantly affected by the strain rates. The compressive strength and ultimate strain in the in-plane direction are obviously lower than those in the normal direction. Under the dynamic compressive load, as the strain rate increased, the strength and elastic modulus increased in both load directions. The main dynamic failure modes of composites in the in-plane direction and in the normal direction are longitudinal splitting and pure compression, respectively. The typical microscopic failures are interfacial crack, fiber fracture and deformation of resin. ZnO whiskers could contribute to the good mechanical properties of composites. The compressive failures of composites are complex and heat could be generated during the loading process.

Acknowledgements

The authors are very grateful to the National Nature Science Foundation of China (Grant No. 10672020) and the Doctoral Fund of Hebei University (Grant No. 2009-148) for providing the research grant.

References

[1] P.J. Falzon and I. Herszberg: Compos. Sci. Technol. Vol. 58 (1998), p. 253

[2] Z.W. Zhou, L.S. Chu and S.C. Hu: Mat. Sci. Eng. B. Vol. 126(2006), p. 93

[3] Z.W. Zhou, S.K. Liu and L.X. Gu: J. Appl. Ploym. Sci. Vol. 80(2001), p. 1520

[4] G.J. Short, F.J. Guild and M.J. Pavier: Compos. Sci. Technol. Vol. 61(2001), p. 2075

[5] H. Kolsky: Proc Phys. Soc. Lond. Vol. 62B (1949), p. 676

[6] Q. Bing and C.T. Sun: Compos. Sci. Technol. Vol. 65(2005), p. 2481

[7] M.V. Hosur, M. Abdullah and S. Jeelani: Mater. Sci. Eng. A. Vol. 445-446(2007), p. 54

[8] M.M. Shokrieh and M.J. Omidi: Compos. Struct. Vol. 89(2009), p.517

[9] D.R. Hufner and M.L. Accorsi: Compos. Struct. Vol. 89(2009), p.177

Advanced Materials Research *Online: 2009-12-21*
ISSN: 1662-8985, Vols. 87-88, pp 11-15
doi:10.4028/www.scientific.net/AMR.87-88.11

Preparation and controlled-release analysis of ethyl cellulose — moxa leaf powder solution microcapsules

Zhang Yang[1], Li li[2], AU Wai-man[2], Yang Ziming[1], He Guanru[1], Deng Sixian[1], Yang Zhuohong[1,*], Joanne W.Y. Chung[3], Thomas K.S. Wong[3]

[1]College of Science, South China Agriculture University, Guangzhou, P.R.China

[2]Institute of Textile and Clothing, The Hong Kong Polytechnic University, Hung Hum, Hong Kong

[3]College of Nursing, The Hong Kong Polytechnic University, Hung Hum, Hong Kong

*Email:yangzhuohong@yahoo.com.cn

Keywords: Ethyl cellulose, moxa leaf powder solution, microcapsules, controlled-release

Abstract: In this paper, moxa leaf powder solution microcapsules are firstly prepared by phase separation of ethyl cellulose. The microcapsule granules prepared are spherical; with good dispersibility and diameters of 10-100μm; have good effects in preservation and prolonged-releasing of active compositions in moxa leaf. The controlled-release experiment proves that after immersing in normal saline for 24 hours under constant temperature of 37°C, releasing amount of the microcapsules is less than 80%, thus the active compositions in moxa leaf still exist in the granules.

1. Introduction

Moxa leaf is a commonly used Chinese medicine and has a long history in China. Chinese have had a great interest in it for hundreds of years, and it was recorded in *Ming Yi Bie Lu* and *Ben Cao Hui Yan*[1,2]. It is traditionally believed that moxa leaf can regulate functional activities and blood circulation; dispel cold and damp; smooth menstruation; prevent miscarriage; kill parasites and relieve itching [3]. It has many effects such as anti-virus, choleretic [4], hemostasis [5] and anti-cancer [6]. Besides, the polysaccharide in moxa leaf can enhance the phagocytic function [7] of reticulo-endothelial cell. Microcapsule technology has been rapidly developed and widely applied in different fields since 1957 [8]. Scientists like Tomofumi[9] prepared the drug microcapsules, which have controlled-release effect within 12 hours, using ethyl cellulose and carboxymethyl cellulose (CMC) as wall-forming materials; others like Prakash[10] prepared the microcapsules using modified cellulose which also have controlled-release effect; Li Guoshu and Bi Wentong[11] conducted researches on preservation of the microcapsule technology and activity of the ethyl cellulose in vitamin C. However, no research has been conducted worldwide yet on the water soluble sandwich material of moxa leaf and its active compositions. In order to solve some limitation in using moxa leaf and its extractive, microcapsule technology is applied in this paper to firstly prepare ethyl cellulose powder microcapsules, with diffusion juice of moxa leaf as the sandwich material. Thus, the effective components of moxa leaf can be preserved and at the same time its strong odor can be staved off.

2. Experiment

2.1. Experimental materials

Ethyl cellulose was purchased from Dongsheng chemical company, P. R. China, Moxa leaf powder was obtained from Peili pharmaceutical company, P. R. China. All other chemicals and reagents used in the study were of analytical grade and obtained from Damao chemical company, P. R. China.

2.2. Preparation of the microcapsules

20% of moxa leaf powder solution (g/g) was prepared by dissolving the powder in water. The clear liquid on the upper layer was acquired by centrifugation for later use. After 2g of ethyl cellulose was completely dissolved in 26g of ethyl acetate, moxa leaf powder solution was added with rotation rate at 2400r/min and was stirred for 10min. 2.16ml of polyethylene glycol, 0.65ml of tween80 and 2.60ml of span80 were added quickly in 20s into 260g of second water. The system was stirred evenly with rotation rate at 1500r/min for 10min and the temperature was kept below 10°C. Lastly the system was pumped out, deposited for 2 hrs and then filtered. After rinsing with water, the preliminary product was dried at 50°C to form white microcapsules powder.

2.3. Experiment on the controlled-release effect of the microcapsule

In this experiment, dynamic dialysis is applied to test the controlled-release of the microcapsule. Dialysis tubing contained 0.2g of microcapsules suspended in 5ml of normal saline was immersed in 100ml of normal saline. The system was oscillated at 100r/min in a 37°C thermostatic oscillator. 10ml of normal saline was drawn out from time to time and 10ml of fresh normal saline was immediately added each time. Using normal saline as a control, the amount of light absorbed in 250nm by the normal saline drawn out was tested. The accumulative controlled-release rate of the microcapsules according to time could be calculated.

3. Results and discussion

3.1. Apparent shape and affecting factors of the microcapsules

In this experiment, scanning election microscope (SEM) is used to observe ethyl cellulose, i.e., apparent shape of moxa leaf powder solution microcapsules. The results are shown below in Fig.1 and Fig.2.

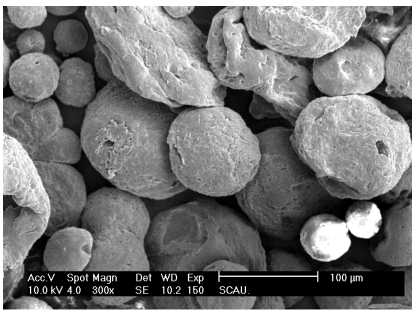

Fig.1 SEM of ethyl cellulose moxa leaf powder solution microcapsules

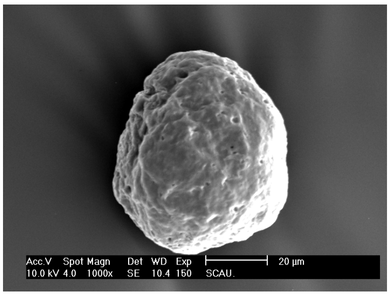

Fig.2 SEM of ethyl cellulose moxa leaf powder solution microcapsules individual

It is observed in Fig.1 and Fig.2 that the microcapsules are in regular spherical or oval shapes and the individual granule diameters distribute to a rather wide range with diameters of 10-100μm. Reasons for the uneven distribution of the granule diameters are: The size distribution of the microcapsule granules is in proportion to the size distribution of granule cores, i.e., the smaller the granule cores are, the smaller the microcapsule granules are. In the experiment, forces exerted on each unit of the system were uneven due to the shape of glassware used. Thus, drop sizes of the sandwich material were unevenly formed. After they were enveloped by the wall-forming material, granules in different sizes were formed finally. Distribution of each unit in the system becomes evener according to time during mixing. If wall thickness of the microcapsules becomes evener gradually, size of the granules will be more stable.

3.2. Controlled-release condition of the microcapsules

3.2.1 Ultraviolet standard curve

100ml constant volumes of different concentration of moxa leaf powder solution were prepared in order to test the amount of light absorbed by each of the concentration. The standard curve was drawn as shown Fig.3, with x-axis is the concentration of moxa leaf powder and y-axis is the amount of light absorbed. Correlation coefficient of the curve is 0.99982 and the linearity is good.

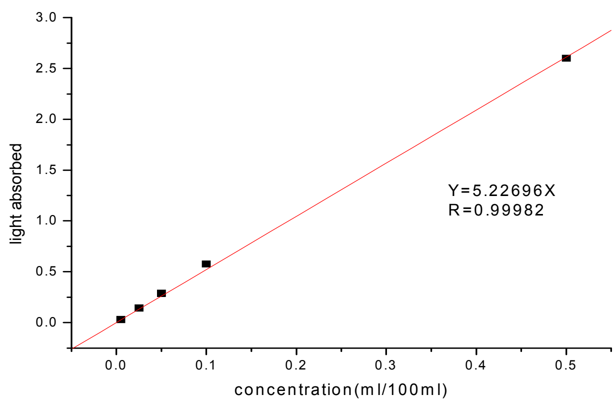

Flg.3 Standard curve for difference concentration of moxa leaf powder solution

3.2.2. Entrapment efficiency and drug loading

Entrapment efficiency and Drug loading was calculated as L.W. Chan [12] suggested: Entrapment efficiency = $w_1/w_2\times100$, Drug loading = $w_1/w_3\times100$, where w_1 is the amount of sandwich material enveloped in certain amount of microcapsules; w_2 is the amount of sandwich material put in the microcapsules with same weight; w_3 is the weight of microcapsules. The results are shown in Tab.1. The results showed that as the more moxa leaf powder solution is added, the higher entrapment efficiency and drug loading of the microcapsules are.

Tab.1 Drug loading and entrapment efficiency of microcapsules

Moxa leaf powder solution [ml]	3	4	5
Drug loading[%]	38.62	51.47	68.59
Entrapment efficiency[%]	22.67	47.50	56.80

3.2.3. Controlled-release result and discussion of the microcapsules

Three different concentrations of moxa leaf powder solution microcapsules were used in the experiment in order to compare the controlled-release results. The release curve of Fig.4 was drawn with x-axis is the releasing time and y-axis is the releasing amount (%).

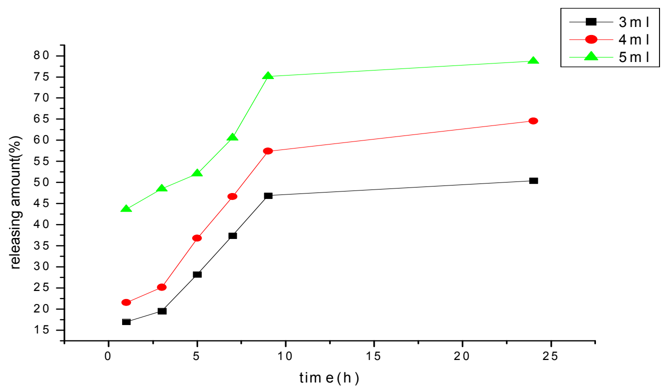

Flg.4 Slow-release curve for moxa leaf powder solution microcapsules

It is shown in Fig.4 that after immersing in normal saline for 24 hours, the active compositions in moxa leaf still exist in the granules according to the releasing amount of the microcapsules is less than 80%.Within the first 9 hours, releasing amount of the microcapsules is greater and at a faster rate. We think that a pure moxa leaf powder solution zone was formed in the center of the microcapsule by envelopment of the sandwich material. Moxa leaf powder solution distributed physically in the microcapsules, or formed a macromolecule/ moxa leaf powder solution system with the wall-forming material. In the primary releasing stage, moxa leaf powder solution on the surface or surface layer is easier to release. Thus, the releasing rate is faster within the first 9 hours, while it slows down afterward. It is also obvious that the releasing amount and releasing rate increase as the volume of moxa leaf powder solution increases. The reason for that may be: since the amount of ethyl cellulose used has been fixed in 2g, wall of the microcapsules prepared becomes thinner and the total surface area increases as the volume of moxa leaf powder solution increases. Thus, diffusion rate of the sandwich material becomes faster and the releasing amount also increases. Moxa leaf solution also contains large amount of mold polysaccharides which is easily oxidized. After leaving the moxa leaf powder solution for 24 hours, mold starts to grow and the solution deteriorates. Therefore, microcapsule technology is applied to solve that problem effectively.

4. Conclusion

In this paper, microcapsules with water-soluble core are firstly prepared by the phrase separation of ethyl acetate-ethyl cellulose. It is proved that the method is workable. Diameters of the microcapsules prepared are 10-100μm. The results showed that overall effect of the microcapsules is good, as utilization rate of the raw materials and preservation rate of the medicine are rather high. The highest drug loading and the highest entrapment efficiency of the microcapsules are 68.59% and 56.80% respectively. It is shown in the controlled-release experiment that releasing rate and releasing amount of moxa leaf powder solution are faster and greater respectively within the first 9 hours, while becomes stable after 10 hours and then increases slowly. After immersing in normal saline for 24 hours, the releasing amount of the microcapsules is less than 80%.Thus, it is clear that ethyl cellulose microcapsule technology is effective in preservation of moxa leaf powder solution activities. Besides, the controlled-release effect of microcapsulized moxa leaf powder solution is conspicuous, thus can prolong the effective time of the solution. Therefore, ethyl cellulose moxa leaf powder solution microcapsules can promote a wide application and development of moxa leaf in medical treatment and daily life because the microcapsules are stable, safe and have controlled-release effect.

Acknowledgements

This work was supported by research grants from the Guangdong Province Science & Technology Program (2006B13801004) and The Hong Kong Polytechnic University.

References

[1] F. Zhou, L.P. Qin, J.F Lian. *Journal of Pharmaceutical Practice.* **18** (2000) 96

[2] Q.M. Xie, R.L. Bian, Q.H Yang. *The Chinese Journal of Modern Applied Pharmacy.* **16** (1999) 16

[3] R. A. Ren. *Authentication of Chinese Medicines[M]*.Shang Hai.**1986**

[4] J.F. Qiu, Z.R. Hu. *Journal of Practical Traditional Chinese Medicine.* **19** (2003) 446

[5] X.L. Zhang. *Journal of Chinese Medicinal Materials.* **15**(1992)22

[6] Q.X. Mei. *Chinese Traditional and Herbal Drugs.* **27 (**1996**)** 311

[7] R.X. Wen, W. Li, X.D. Zhou. *China Journal of Chinese Materials Medicine.* **17** (1992) 406

[8] B. K. Green, L. Schleicher. *U S patent* **2800457** (1957)

[9] Y. Tomofumi and O. Hiraku. *Journal of Controlled Release*. **75** (2001) 271

[10] M. Guyot and F. Fawaz. *Journal of Pharmaceutics.* **175** (1998) 61

[11] G.S. Li and W.T. Xue *Science and Technology of Food Industry.*, **26** (2005) 41

[12] L.W. Chan, L .T. Lim, P.W.S. Heng. *Journal of Microencapsulation.* **17 (2000) 757**

Advanced Materials Research *Online: 2009-12-21*
ISSN: 1662-8985, Vols. 87-88, pp 16-21
doi:10.4028/www.scientific.net/AMR.87-88.16

Numerical Simulation of Temperature Field in Barrel of Injection Molding Machine during Induction Heating Process Based on ANSYS Software

Chang Shijia[1,a], Xie Pengcheng[1,b], He Xuetao[1,c], Yang Weimin[1,d]

[1]College of Mechanical and Electrical Engineering, Beijing University of Chemical Technology, Beijing, China

[a]changshijia.3932@yahoo.com.cn, [b]xiepengcheng@gmail.com, [c]hext@mail.buct.edu.cn, [d]yangwm@mail.buct.edu.cn

Keywords: injection molding machine; induction heating; ANSYS; numerical simulation; electromagnetic field; temperature field

Abstract: A finite element model of temperature field coupled with electromagnetic field has been established based on induction heating theory including Maxwell's equations, thermal conductivity differential equation and magnetic vector potential to simulate the induction heating process of barrel of injection molding machine by universal ANSYS software, and to obtain temperature field of the barrel related to time variation. The coupled thermal and electromagnetic field problem taking account of nonlinear materials characteristics related to temperature was discussed. The induction heating process of barrel was analyzed, and the temperature distribution and its variation with time were obtained.

1 Introduction

Plastic injection molding is to inject the melt plastics into the mold, through cooling and curing methods to form molding products. Barrel temperature of injection molding machine is an important process parameters. At present, heating method of the barrel of the injection molding machine is usually resistance heating which fix several resistance heating coils on the out-surface of barrel, and the temperature of each heating coil can be independently controlled. This paper will apply the induction heating technology to injection molding machine. Induction heating has many advantages, such as high heating speed, high barrel internal heating and heating efficiency, uniform and selective heating, less environmental pollution, well-controlling, safety. Based on the principle of induction heating induced current (eddy current) distribution has skin effect in the barrel surface, that is concentrated in a small range of barrel surface, the barrel temperature is going up by the internal heat transfer. Induction heating is a complex physical process with coupling electromagnetic field and temperature field. In the heating process magnetic permeability, electrical conductivity, specific heat capacity and other physical parameters of the barrel material will vary with temperature, and these factors in turn, will have an impact on the heating process. In addition, injection molding machine of induction heating as compared to the present industrial application of induction heating has its own features:(1) Barrel temperature is lower, generally around 200℃;(2) Barrel heating time is longer, as the barrel temperature need high precision, in order to facilitate temperature control, so barrel temperature must rise stably;(3) Lower heating power, lower frequency and barrel temperature, higher precision of temperature control and longer heating time all require an inductor to have appropriate power and frequency. In summary, this paper that analyzes and studies induction heating process of the barrel of injection molding machine using ANSYS can optimize design parameters of inductor.

2 Governing equations for electromagnetic field

2.1 Mathematical model of magnetic field

The governing equations for time varying magnetic field analysis can be derived from Maxwell's equations[1]:

$$\begin{cases} \nabla \times \vec{H} = \vec{J} \\ \nabla \times \vec{E} = -\dfrac{\partial \vec{B}}{\partial t} \\ \nabla \cdot \vec{D} = 0 \\ \nabla \cdot \vec{B} = 0 \end{cases} \tag{1}$$

The constitutive equations are

$$\begin{cases} \vec{B} = \mu \vec{H} \\ \vec{J} = \vec{J_e} + \vec{J_s} = \sigma \vec{E} + \vec{J_s} \\ \vec{D} = \varepsilon \vec{E} = \varepsilon_0 \varepsilon_r \vec{E} \end{cases} \tag{2}$$

ANSYS software uses the method of the magnetic vector potential to calculate electromagnetic field and eddy current field. Introducing $\vec{B} = \nabla \times \vec{A}$, $\vec{A}$ is the magnetic vector potential. When the source current density varies by the sine curve with time, ignoring high-order harmonic of each variable, it can be calculated by plural terms, changing the corresponding scalar field into a complex scalar and the corresponding vector field into a complex vector[2]. We get

$$\nabla \times \frac{1}{\mu} \nabla \times \vec{A} = -j\omega\sigma \vec{A} + \vec{J_s} \,. \tag{3}$$

Where ω is the prescribed angular frequency. Eq.(3) is the solution of eddy current field of differential equations of the complex vector.

2.2 Mathematical model of temperature field

From the heat diffusion equation in cylindrical coordinates and for the axisymmetric case, the conduction in the barrel is governed by the equation[3]:

$$\frac{1}{r}\frac{\partial}{\partial r}\left(rk\frac{\partial T}{\partial r}\right) + \frac{\partial}{\partial z}\left(k\frac{\partial T}{\partial z}\right) + q_v = \rho c \frac{\partial T}{\partial t} \,. \tag{4}$$

3 Finite element numerical simulation model

3.1 Numerical simulation model

This paper discusses induction heating of the cylindrical barrel, on which there are 3-7segments induction heating coil winding. In the temperature throughout the barrel of injection molding machine, the maximum temperature of inner wall of the barrel has a direct impact on the quality of products, so the only need is to model for the middle part of the barrel wrapped by each induction coil. The physical parameters of the actual electromagnetic field and temperature field are the distribution of symmetry throughout the circumferential direction of barrel, assuming uniform and continuous (isotropic) barrel material, so the actual three-dimensional model can be reduced to two-dimensional processing; Further assume that a segment of the middle part of the barrel wrapped induction heating coil only has radial thermal conduction, and there is no axial heat conduction. Therefore, the induction heating problem of the barrel can further be simplified as one-dimensional problem, and efficiency of calculation will be greatly enhanced. Fig.1 shows one-dimension simulation model of induction heating representing the barrel.

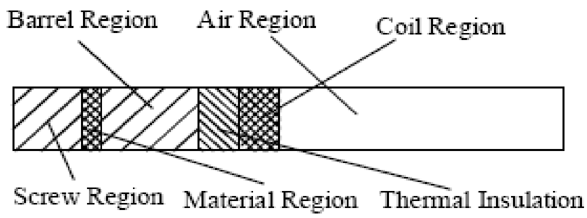

Fig.1 One-dimension simulation model of induction heating

3.2 Loads, boundary conditions and meshing

Boundary conditions of the simulation of electromagnetic field are that the magnetic potential is zero at the edge of far field (infinite distance), and the magnetic line is parallel to the axis of barrel. Load conditions of uniform source current density (the coil of the cross-sectional area divided by current intensity) are applied on the section of the induction coils, and the conditions at the same time are the incentive conditions of electromagnetic fields. Fig. 2(a) shows the boundary conditions of electromagnetic field; Radiation boundary condition is applied on the barrel surface (heat convection is negligible). Fig. 2(b) presents the boundary conditions of thermal field.

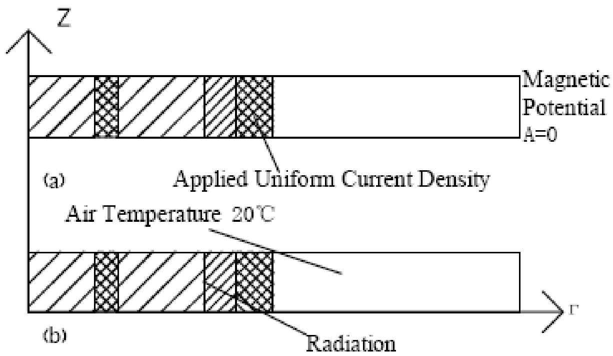

Fig.2 Boundary condition of the electromagnetic field (a) and the thermal field (b)

In numerical simulation with finite element, the mesh quality has a direct impact on the accuracy of the calculation results, as well as the efficiency of the calculation. Fig. 3 shows finite element mesh dividing of the model.

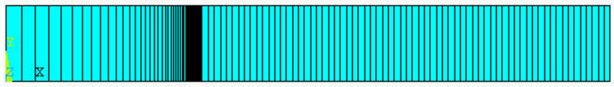

Fig.3 Finite element mesh dividing of the model

3.3 Realization of temperature field coupled with electromagnetic field

In ANSYS software, the distribution of electromagnetic field and temperature field is affected by the physical parameters of material which are varied with temperature. This paper uses the "method of physical environment" to calculate the two-way coupling between the electromagnetic-heat. Fig.4 shows the solution flow diagram for electromagnetic-thermal coupled-field.

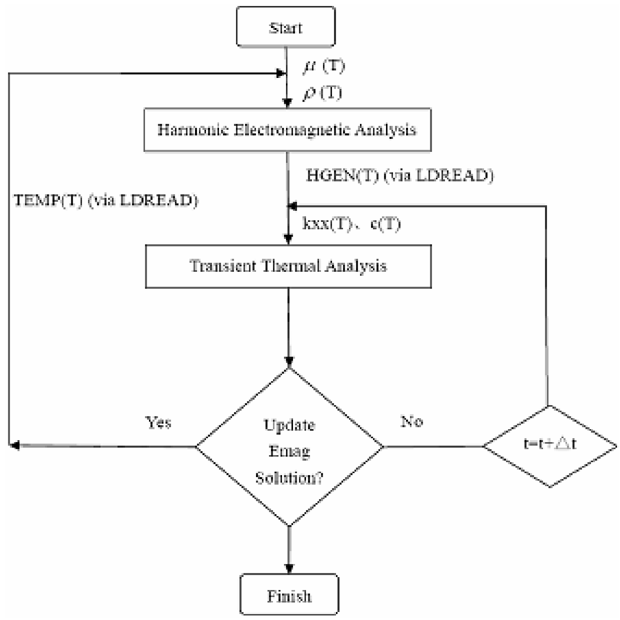

Fig.4 Solution flow diagram for electromagnetic-thermal coupled-field

4 Simulation and analysis of the actual working status

4.1 Simulation object and calculation parameters

Select one segment of the barrel of injection molding machine as the simulation object, then simulate the heating process of this segment. The main parameters are the power of 3kW, the frequency of 20kHz, the coil diameter of 150mm, coil cross-section of 240mm × 10mm, the current density of $5\times10^5 A/m^2$, the barrel material of 45 steel, barrel inner diameter of 60mm, barrel outer diameter of 130mm, Barrel initial temperature and ambient temperature of 20℃, the radiation factor of 0.2.

4.2 Simulation results and analysis

Fig.5 shows the finite element simulation results of the temperature field of induction heating of the injection molding machine barrel. According to Fig.5, after 500 seconds the temperature difference between the barrel wall and the barrel surface is 16.45℃. At the same time, the maximum temperature occurs on barrel's surface, which mainly results from the insulating layer above the barrel surface, resulting in few of heat dissipation of surface.